

CONTENTS

| | | |
|--------|--|----|
| 1 | NARROW LINE REGION PROPERTIES | 1 |
| 1.1 | Introduction | 1 |
| 1.2 | Quasar Sample | 2 |
| 1.2.1 | Low- z sample | 3 |
| 1.3 | Parameteric Model Fits | 3 |
| 1.3.1 | Model One: Multiple Gaussians | 4 |
| 1.3.2 | Derived parameters | 5 |
| 1.3.3 | Absolute flux calibration of spectra and continuum luminosities | 7 |
| 1.3.4 | Reliability of derived parameters | 7 |
| 1.3.5 | Model Two: Independent Component Analysis | 11 |
| 1.3.6 | Physical interpretation of Independent component analysis (ICA) components | 12 |
| 1.4 | Results | 14 |
| 1.4.1 | Gaussian fits | 14 |
| 1.4.2 | ICA fits | 18 |
| 1.5 | Measuring the quasar systemic redshift | 24 |
| 1.5.1 | H α | 24 |
| 1.5.2 | ICA | 26 |
| 1.6 | Luminosity/redshift-evolution of [O III] properties | 26 |
| 1.7 | Equivalent width | 28 |
| 1.7.1 | [O III] and C IV outflows are linked | 29 |
| 1.8 | Eigenvector one correlations | 31 |
| 1.9 | Broad Absorption Line Quasars | 31 |
| 1.10 | Discussion | 31 |
| 1.10.1 | Type II quasars | 31 |

LIST OF FIGURES

- Figure 1.1 Multi-component Gaussian fits to the continuum-subtracted $H\beta/[O\text{III}]$ emission in 15 quasars, chosen at random. The data is shown in grey, the best-fitting parametric model in black, and the individual model components in orange. The peak of the $[O\text{III}]$ emission is used to set the redshift, and Δv is the velocity shift from the line rest-frame transition wavelength for $H\beta$. Below each fit we plot the data minus model residuals, scaled by the errors on the fluxes. 6
- Figure 1.2 Continuum- and Fe II -subtracted spectra of the 23 objects we identified where the Boroson and Green, (1992) empirical template is a poor match to the Fe II emission. The vertical lines indicate the expected positions of the $[O\text{III}]$ doublet (which is generally very weak) with the systemic redshift defined using the peak of the broad $H\beta$ emission. 8
- Figure 1.3 Distribution of $[O\text{III}]\lambda 5008$ equivalent width (EQW). The $[O\text{III}]$ profiles of the 120 objects in the red bin ($\text{EQW} < 8\text{\AA}$) cannot be measured reliably. 9
- Figure 1.4 Change in the $[O\text{III}]$ line parameter w_{80} as the signal-to-noise (S/N) is artificially varied from 3-50 for two different objects. At each S/N, our line-fitting procedure is run on 100 mock spectra, and the points and errorbars indicate the 50th percentile and 16-84 percentile range respectively. The spectra is flagged if $|\Delta w_{80}| > 0.1$ at the S/N of the spectra (shown by the vertical line). 10
- Figure 1.5 ICA reconstruction of J002952+020607. The ICA reconstruction is shown in black, and the spectrum in grey. The first three components, and the sum of components four, five and six are shown individually. 13

- Figure 1.6 [O III] emission in J002952+020607. The data is shown in blue, and the ICA spectrum in grey. The first three ICA components have been subtracted from both the ICA composite and the data. The black curve shows the reconstructed [O III] profile (see text). 14
- Figure 1.7 Correlations between w_{80} , R and EQW of [O III]. 119 objects are included: objects with low EQW, poor S/N, poor Fe II subtraction are not included. Objects for which [O III] is modelled using a single Gaussian are also excluded, because the asymmetry is always zero for these objects. 15
- Figure 1.8 The high- z Eigenvector 1 (EV1) parameter space of C IV blueshift and EQW. Our sample is shown with points, and quasars from the full Sloan Digital Sky Survey (SDSS) catalogue are shown with grey contours. The [O III] EQW varies systematically with position in the C IV blueshift-EQW parameter space (a) but H β FWHM shows significantly less systematic variation (b). 17
- Figure 1.9 Multi-component Gaussian fits to the continuum-subtracted H β /[O III] emission in 18 quasars with extreme [O III] emission profiles. 19
- Figure 1.10 The relative weight in each of the six positive ICA components for the high-luminosity (blue) and low luminosity samples (grey). In the high-luminosity sample Fe II emission is stronger (component w_1). The core [O III] emission (components w_4 , w_5) is weaker but the strength of the blueshifted wing (w_6) is the same. 20
- Figure 1.11 The relative weight in the three ICA components corresponding to [O III] emission (*left*) and the relative weight of the component most closely related to blueshifted [O III] emission relative to all three [O III] components (*right*). [O III] emission is weaker in the high-luminosity sample, but the relative contribution from the blueshifted component to the total [O III] emission is higher. 21
- Figure 1.12 Anti-correlation between the relative contribution from the wing to the total [O III] profile and the strength of the core. 21

- Figure 1.13 The strength of core [O III] as a function of the C IV blueshift. The C IV blueshift is measured relative to the NIR ICA redshift. 22
- Figure 1.14 The strength [O III] EQW as a function of the C IV blueshift. The C IV blueshift is measured relative to the NIR ICA redshift. 22
- Figure 1.15 Median ICA-reconstructed spectra as a function of the C IV blueshift. 23
- Figure 1.16 Comparison of systemic redshift estimates using [O III], broad H β and broad H α . In all cases the line location is defined as the peak wavelength of the best-fitting model. There are 93, 73 and 83 objects in (a), (b) and (c) respectively. The mean and standard deviation have been calculated by fitting a Gaussian function to the distribution. **Need to look at flags>1 for H α and H β . Is peak around zero in (a) real?** 25
- Figure 1.17 The [O III] velocity-width, characterised by w_{80} , as a function the [O III] luminosity and the quasar redshift. The color of each hexagon denotes the mean w_{80} for the objects in that luminosity-redshift bin. We have supplemented our sample with low- z objects from Zakamska and Greene, (2014) and medium ($z \sim 1.5$) redshift objects from Harrison et al., (2016). If I keep this plot make sure its clear which points belong to which sample. 27
- Figure 1.18 The [O III] EW as a function of the quasar bolometric luminosity for the sample presented in this chapter (blue circles) and the low- z SDSS sample (grey points and contours). Upper limits are denoted by the downward arrows. 28
- Figure 1.19 The relation between the blueshifts of C IV and [O III]. Note that we are using v_{10} for the [O III] position and v_{50} for the C IV position. We can't use v_{50} for [O III] because sometimes we are using a single Gaussian, especially if the [O III] is weaker and we miss the broad component. 30

LIST OF TABLES

| | |
|-----------|--|
| Table 1.1 | The numbers of quasars with [O III] line measurements and the spectrographs and telescopes used to obtain the near-infrared spectra. 3 |
| Table 1.2 | Physical interpretation of the ICA components. 13 |
| Table 1.3 | Models used for H α emission 26 |

LISTINGS

ACRONYMS

| | |
|-----------------|--------------------------------|
| AGN | Active galactic nuclei |
| NLR | Narrow line region |
| BLR | Broad line region |
| EV ₁ | Eigenvector 1 |
| ICA | Independent component analysis |
| SDSS | Sloan Digital Sky Survey |
| UV | ultra-violet |
| EQW | equivalent width |
| S/N | signal-to-noise |

NARROW LINE REGION PROPERTIES

1.1 INTRODUCTION

Active galactic nuclei (AGN) are very efficient at driving outflows; X-ray and ultra-violet (UV) spectroscopy reveal high velocity outflows to be nearly ubiquitous on sub-parsec scales in high accretion rate quasars. In recent years, a huge amount of resources have been devoted to searching for observational evidence of galaxy-wide, AGN-driven outflows, which could provide the feedback mechanism necessary to quench star formation in massive galaxies. This has resulted in recent detections of winds in AGN-host galaxies using tracers of atomic, molecular, and ionised gas (e.g. Nesvadba et al., 2006; Arav et al., 2008; Nesvadba et al., 2008; Moe et al., 2009; Dunn et al., 2010; Alexander et al., 2010; Harrison et al., 2012; Harrison et al., 2014; Nesvadba et al., 2010; Rupke and Veilleux, 2013; Veilleux et al., 2013; Nardini et al., 2015; Feruglio et al., 2010; Alatalo et al., 2011; Cimatti et al., 2013; Cicone et al., 2014).

One particularly successful technique has been observations of forbidden emission lines, which trace warm ($T \sim 10^4$ K) ionised gas in the Narrow line region (NLR). Because of its high equivalent width, $[\text{O III}]\lambda 5008$ is most studied of the narrow quasar emission lines. In general, the $[\text{O III}]$ emission appears to consist of two components: a narrow, ‘core’ component, with a velocity close to the systemic redshift of the host galaxy, and a broader ‘wing’ component, which is normally blueshifted. The general consensus is that the core component traces the gravitational potential of the host galaxy, as the width correlates well with the stellar velocity dispersion. On the other hand, the wing is tracing outflowing gas. This can be explained if the far-side of any outflowing gas, that is moving away from the line of sight, is obscured by dust in the host galaxies (e.g. Heckman et al., 1981; Vrtilek, 1985).

Observations of broad velocity-widths and asymmetries in narrow emission lines stretch back several decades (e.g. Weedman, 1970; Stockton, 1976; Heckman et al., 1981; Veron, 1981; Feldman et al., 1982; Heckman, Miley, and Green, 1984; Vrtilek, 1985; Whittle, 1985; Boroson and Green, 1992). However, the small sample sizes make it difficult to know how representative these observations are. More recently, the advent of large optical spectroscopic surveys (e.g. SDSS) have facilitated studies of the NLR in tens of thousands of AGN (e.g. Boroson, 2005; Greene and Ho, 2005; Zhang et al., 2011; Mullaney et al., 2013; Zakamska and Greene, 2014; Shen and Ho, 2014). This has

provided constraints on the prevalence of ionised outflows and, by measuring outflow properties as a function of AGN properties, on the drivers of these outflows. At the same time, there is strong evidence from spatially resolved spectroscopic observations of kinematically disturbed gas extended over galaxy scales (e.g. Greene et al., 2009; Greene et al., 2011; Hainline et al., 2013; Harrison et al., 2012; Harrison et al., 2014).

However, these studies do not cover the redshift range when star formation and black hole accretion peaked, and consequently when feedback is predicted to be strongest. At these redshifts the bright optical emission lines are redshifted to near-infrared wavelengths, where observations are much more challenging compared to optical wavelengths. As a consequence, studies at high redshifts have typically relied on relatively small numbers of objects, which might not be representative of the properties of the population (e.g. Netzer et al., 2004; Sulentic et al., 2004; Shen, 2016). Other recent studies have looked at the [O III] emission properties of rare sub-samples - e.g. heavily obscured quasars (Zakamska et al., 2016) and the most luminous quasars (Bischetti et al., 2016). These studies often report exceptionally large [O III] widths, with $\text{FWHM} > 1000 \text{ km s}^{-1}$ (e.g. Netzer et al., 2004; Nesvadba et al., 2008; Kim et al., 2013; Brusa et al., 2015; Carniani et al., 2015; Perna et al., 2015; Bischetti et al., 2016). This could suggest that AGN efficiency in driving galaxy-wide outflows increases with AGN luminosity. In addition, [O III] is often very weak, or is missing entirely (e.g. Netzer et al., 2004).

In this chapter we analyse the [O III] properties of a sample of 356 high-luminosity, redshift $1.5 < z < 4$ quasars. The large sample size will help to put these observations in context of the AGN population as a whole. We will analyse the [O III] emission properties as a function of key properties of the quasar, e.g. BH mass, luminosity, and accretion rate.

1.2 QUASAR SAMPLE

We have assembled a catalogue of 356 high-luminosity, redshift $1.5 < z < 4$ quasars. These are selected from our near-infrared spectroscopic database (Chapter 2) to have spectra covering the strong, narrow [O III] doublet. The broad Balmer $\text{H}\beta$ line is also observed for all but two of the sample. In 165 the spectra extend to the broad $\text{H}\alpha$ emission at 6565 \AA , and in 260 optical spectra including C IV are also available (mostly from SDSS/BOSS). This is the largest study of the narrow line region properties of high- z quasars ever undertaken. The quasar sample is summarised in Table 1.1.

Table 1.1: The numbers of quasars with [O III] line measurements and the spectrographs and telescopes used to obtain the near-infrared spectra.

| Spectrograph | Telescope | Number |
|--------------|-----------|--------|
| FIRE | MAGELLAN | 31 |
| GNIRS | GEMINI-N | 28 |
| ISAAC | VLT | 9 |
| LIRIS | WHT | 7 |
| NIRI | GEMINI-N | 29 |
| NIRSPEC | Keck II | 3 |
| SINFONI | VLT | 80 |
| SOFI | NTT | 76 |
| TRIPLESPEC | ARC-3.5m | 27 |
| TRIPLESPEC | P200 | 45 |
| XSHOOTER | VLT | 21 |
| | | 356 |

1.2.1 Low- z sample

To test for variation in the [O III] emission line properties with redshift and/or luminosity, we use a sample of quasars selected from the SDSS. .

Details of sample

1.3 PARAMETERIC MODEL FITS

In this section we describe how parameters of the [O III] emission are derived. Our approach is to first model the spectra, and then derive parameters of interest from the best-fitting model. This enhances the useful information that can be extracted from spectra with finite S/N.

Two different models are considered. The first consists of a power-law continuum, an empirical Fe II template and multiple Gaussian components to model the emission from the broad and narrow components of H β and the [O III] doublet. This is a model which is commonly adopted in the literature (e.g. Shen et al., 2011). The second model consists of six spectral components derived from an ICA of a large sample of low-redshift AGN with SDSS spectra covering the same spectral region. As we will demonstrate, a linear combination of these spectral components is able to reproduce the spectra around H β /[O III] to a high degree of precision.

1.3.1 *Model One: Multiple Gaussians*

The first step in our procedure is to fit a combination of a power-law continuum and an optical Fe II template – taken from Boroson and Green, (1992) – to two windows at 4435-4700 and 5100-5535 Å. The Fe II template is convolved with a Gaussian, and the width of this Gaussian, along with the normalisation and velocity offset of the Fe II template, are free variables in the pseudo-continuum fit.

This requires the spectra to be transformed to within $\sim 1000 \text{ km s}^{-1}$ of the quasar rest-frame. The redshift used in this transformation is either derived from the peak of the broad H α emission (~ 40 per cent of our sample), from the peak of the broad H β emission (~ 40 per cent) or from the peak of the narrow [O III] emission (20 per cent). In later sections, emission line locations will always be quoted as relative velocities, and so do not explicitly depend on how the quasar rest-frame is defined at this stage in the fitting procedure.

Once the continuum and Fe II emission has been modelled and removed, the following model is fit in the wavelength interval 4700-5100 Å. The fit is done as a function of the Doppler velocity shift, and we adopt the wavelength 4862.721 Å (the laboratory H β wavelength) to transform wavelengths into equivalent Doppler velocities.

In general, H β is modelled by two Gaussians with non-negative amplitudes and FWHM greater than 1200 km s^{-1} . In 10 objects H β is modelled with a single Gaussian and in 41 objects H β is modelled with two Gaussians, but the velocity centroids of the two Gaussians are constrained to be equal. These spectra generally have low S/N, and adding extra freedom to the model does not significantly decrease the minimised reduced chi-squared. In addition there are cases where the blue wing is below the lower wavelength limit of the spectrograph; in these cases models with more freedom are insufficiently constrained by the data with limited wavelength coverage.

Contributions to the H β emission from the narrow-line region is weak in the vast majority of our sample, and in general we do not include an additional Gaussian component to model this emission. In 9 objects features in the model - data residuals suggest that a narrow emission component is significant, and an additional narrow Gaussian is included for these quasars. It is likely that there is some not insignificant contribution from the narrow line region in other quasars. If this is the case then measures of the H β velocity width will be biased to lower values on average. However, in this chapter we are only interested in location of the peak of the H β emission (to infer the quasar redshift). This is unlikely to be biased by not decomposing the narrow and broad emission components.

Each component of the [O III] doublet is fit with one or two Gaussians, depending on the fractional reduced χ^2 difference between the one- and two-component models. If the addition of the second

Gaussian decreases the reduced χ^2 by more than 5 per cent then the double-Gaussian model is accepted. One hundred and thirty-one are fit with a single Gaussian and 154 with two Gaussians. When a single Gaussian is used to model each line, the peak flux ratio of the [O III] 4960 Å and 5008 Å components are fixed at the expected 1:3 ratio and the width and velocity offsets are set to be equal. In the double Gaussian fit, the peak flux ratio of the second components is again fixed at 1:3, and the width and velocity offsets are again set to be equal.

In 71 objects [O III] is undetected, or is very low S/N. In these cases we do not attempt to measure the width of the [O III] emission, but instead fit a fixed [O III] template, only the overall normalisation of which is allowed to vary. The template is derived by running our fitting routine on a very high S/N composite spectra of low redshift AGN.

Model parameters were derived using a standard variance-weighted least-squares minimisation procedure employing the Levenberg-Marquardt algorithm. Prior to the fit, the spectra were inspected visually and regions significantly affected by telluric absorption or of low S/N were masked out. Some example fits are shown in Figure 1.1

Composite details?

1.3.2 Derived parameters

All [O III] line properties are derived from the [O III]5008 emission, but, as described above, the kinematics of the peak at 4960 Å are constrained by our fitting routine to be identical.

We do not attach any physical meaning to the individual Gaussian components used in the model. While it is true that in some quasars the [O III] emission can be clearly separated into a narrow component at the systemic redshift and a lower-amplitude, blueshifted broad component (e.g. Shen, 2016), often this decomposition is highly uncertain and dependent on the spectral S/N, resolution etc. In addition, there is no theoretical justification that wing component should have a Gaussian profile.

We therefore choose to characterize the [O III] line profile using a number of non-parameteric measures, which are commonly used in the literature (e.g. Zakamska and Greene, 2014; Zakamska et al., 2016). A normalised cumulative velocity distribution is constructed from the best-fitting model, from which the velocities below which 5, 10, 25, 50, 75, 90, and 95 per cent of the total flux accumulates can be read off. The width of the emission line can then be defined, for example, using $w_{80} = v_{90} - v_{10}$. The absolute asymmetry in the line profile A is defined as $((v_{95} - v_{50}) - (v_{50} - v_5)) / (v_{95} - v_5)$ (Zakamska and Greene, 2014). We use the peak of the full [O III] profile to define the systemic redshift, and verify below that this is unbiased.

The line width measures are not corrected for instrumental broadening

Add outline of table of derived properties for this chapter

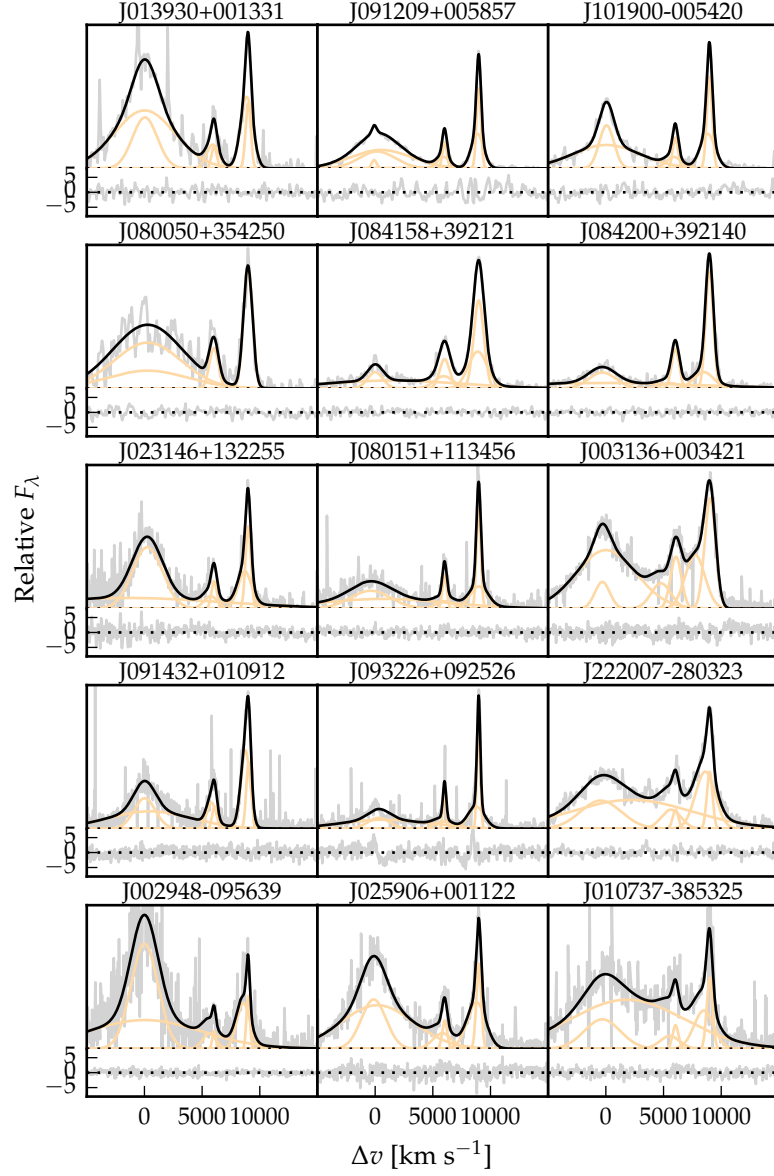


Figure 1.1: Multi-component Gaussian fits to the continuum-subtracted $H\beta/[O\text{ III}]$ emission in 15 quasars, chosen at random. The data is shown in grey, the best-fitting parametric model in black, and the individual model components in orange. The peak of the $[O\text{ III}]$ emission is used to set the redshift, and Δv is the velocity shift from the line rest-frame transition wavelength for $H\beta$. Below each fit we plot the data minus model residuals, scaled by the errors on the fluxes.

1.3.3 Absolute flux calibration of spectra and continuum luminosities

Relative flux-calibration of the infrared spectra as a function of wavelength has been achieved, to $\simeq 10$ per cent, through observations of appropriate flux standards. The absolute flux levels, however, can be in error by large factors due to variable atmospheric conditions combined with the narrow slit widths. For the majority of the quasars we have, therefore, established the absolute flux scale for each near-infrared spectrum using the same quasar SED-model fitting scheme employed in Chapter ???. Briefly, the SED-model was fit, with the normalisation and $E(B-V)$ as free variables, to optical/infrared magnitudes, or SDSS/BOSS spectra (check order I do this.) This allows us to extrapolate from the optical when we do not have photometric data in the near-infrared. The spectra were then normalised to the SED model using a linear error-weighted least-squares regression in the regions of the spectra covered by the H/K bands. The monochromatic continuum luminosity at 5100\AA was calculated directly from the normalised SED-model.

Check if any missing normalisation / monochromatic luminosities.

I think a lot of this is repeated from chapter 2/3

Check factor of $(1+z)$ in luminosity calculation

1.3.4 Reliability of derived parameters

1.3.4.1 Removal of Fe II emission

While we were able to satisfactorily model the Fe II emission in the vast majority of cases, we encountered a number of cases where the relative strengths of the Fe II lines appear to differ significantly from those of I Zw 18 on which the Fe II template is based. As a result, significant Fe II flux remained in the spectrum after the removal process. This emission is at rest-frame wavelengths very close to the [O III] emission, and so could potentially lead to large errors in the inferred [O III] line parameters.

In Figure 1.2 we plot the spectral region around [O III] for 23 quasars we have identified where significant features remain following the subtraction of the continuum and Fe II. The vertical lines indicate the expected positions of the [O III] doublet, with zero velocity defined using the peak of the broad H β emission. [O III] is generally extremely weak in these objects. As a result, the widely-adopted procedure of fitting multiple Gaussians will tend to fit the Fe II emission as broad, shifted [O III]. For example, J125141+080718 was studied by Shen, (2016), and assigned an extremely large [O III] blueshift. Our analysis suggests that this emission is more likely to be Fe II. Because of the difficulty measuring the [O III] properties of these objects, they are excluded from subsequent analysis.

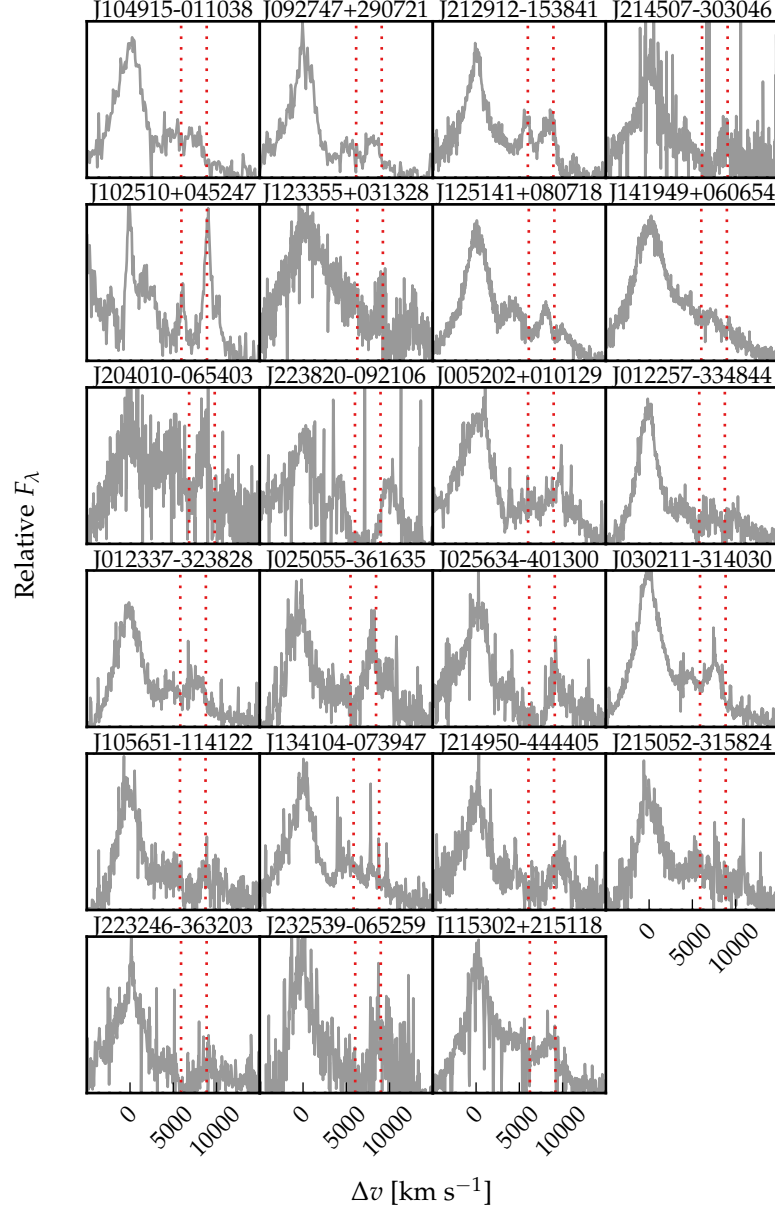


Figure 1.2: Continuum- and Fe II-subtracted spectra of the 23 objects we identified where the Boroson and Green, (1992) empirical template is a poor match to the Fe II emission. The vertical lines indicate the expected positions of the [O III] doublet (which is generally very weak) with the systemic redshift defined using the peak of the broad H β emission.

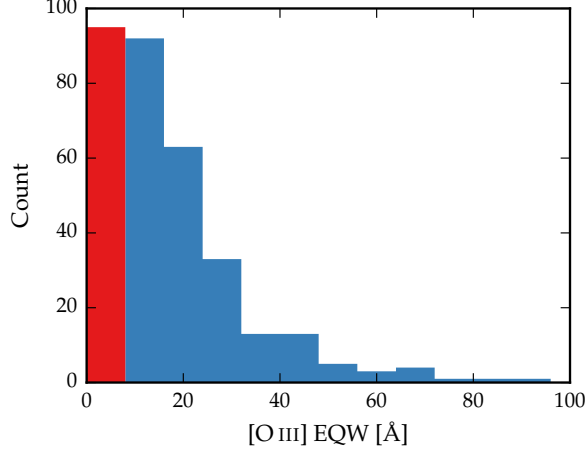


Figure 1.3: Distribution of $[\text{O III}]\lambda 5008$ EQW. The $[\text{O III}]$ profiles of the 120 objects in the red bin ($\text{EQW} < 8\text{\AA}$) cannot be measured reliably.

1.3.4.2 Low EQW $[\text{O III}]$

In Figure 1.3 we show the distribution of the $[\text{O III}]$ rest-frame EQW distribution for the 330 objects in our sample (objects where Fe II emission has been sub-optimally removed are excluded). In many objects $[\text{O III}]$ is undetected. In others it is detected, but is too weak for its shape (i.e. the width and asymmetry) to be measured reliably. We define $\text{EQW} = 8\text{\AA}$ as the limit below which we can no longer reliably determine the shape of the $[\text{O III}]$ emission. Objects with $\text{EQW} < 8\text{\AA}$ (120) are excluded in subsequent analysis of the $[\text{O III}]$ shape.

1.3.4.3 Low S/N $[\text{O III}]$

In this section we flag objects with poor spectral S/N . A single S/N cut is not adequate: for a given S/N , it is much easier to measure the properties of a strong line than a weaker one. Our approach is therefore as follow:

1. For each object use the best-fitting parametric model as a high S/N representation of the spectra.
2. Scale the error spectrum so that the S/N (measured in the continuum and quoted per pixel) is $\{2.5, 5, 7.5, 10, 15, 20, 50\}$.
3. At each S/N , generate 100 mock spectra by randomly drawing the flux in each pixel from a Normal distribution with mean μ equal to the model flux and width σ equal to the scaled error.
4. Run line-fitting procedure on each mock of the 100 mock spectra; record the value of w_{80} in the best-fitting model.
5. Calculate the 16th, 50th and 84th percentiles of the distribution of w_{80} values.

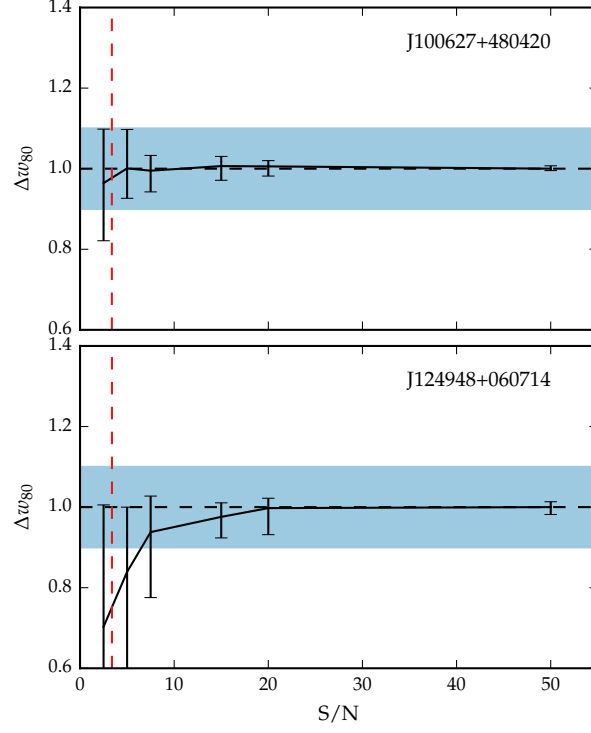


Figure 1.4: Change in the [O III] line parameter w_{80} as the S/N is artificially varied from 3-50 for two different objects. At each S/N, our line-fitting procedure is run on 100 mock spectra, and the points and errorbars indicate the 50th percentile and 16-84 percentile range respectively. The spectra is flagged if $|\Delta w_{80}| > 0.1$ at the S/N of the spectra (shown by the vertical line).

6. A low S/N flag is assigned to the object if the value of w_{80} changes by more than 10 per cent from the highest S/N representation to the S/N of the data.

Two examples are shown in Figure 1.4. The marker denotes the 50th percentile, and the lower and upper error bars the 16th and 84th percentiles respectively. As expected, the uncertainty on w_{80} increases as the S/N of the spectrum decreases. The S/N in to two spectra are similar, but the [O III] line in the first object is stronger. Hence it can still be measured reliably even at low S/N. The first object would pass our S/N cut, whereas the latter would fail.

1.3.5 Model Two: Independent Component Analysis

ICA is a blind source separation technique for separating a signal into linearly mixed statistically independent subcomponents. Unlike the more widely-used principle component analysis technique, ICA produces non-negative components which allows for a physical interpretation of the components and weights. ICA has been successfully applied to model the spectra of emission-line galaxies (Allen et al., 2013) and BAL quasars (Allen et al., 2011). The quasar spectra can be thought of as a set of observations, \mathbf{x} , which are made up of statistically independent components, \mathbf{c} , that are combined by some mixing matrix, \mathbf{W} :

$$\mathbf{x} = \mathbf{W}\mathbf{c} \quad (1.1)$$

ICA reverses this process and describes how the observed data are generated. Both the independent components and the mixing matrix are unknown, but can be found by solving:

$$\mathbf{c} = \mathbf{W}^{-1}\mathbf{x}. \quad (1.2)$$

The components were solved for using a sample of 2,154 SDSS quasars at redshifts XX. At these redshifts the SDSS spectrograph covers the rest-frame region XX-XXÅ where H β and [O III] lie. The individual spectra were first adjusted to give the same overall shape as a model quasar template spectrum. Six positive independent components and four additional components that could be negative were found to be sufficient to reconstruct the spectrum, without overfitting. Each quasar spectrum can then be represented as a linear combination of the independent components:

Ask Paul for details.

$$x_j = \sum_{i=1}^{10} c_{ij} W_{ij} \quad (1.3)$$

1.3.5.1 *Fitting procedure*

For each quasar in our NIR sample we perform a variance-weighted least-squares minimisation to determine the optimum value of the components weights. The fitting procedure we employ is as follows. A power-law is first fit to the quasar template spectrum in emission line free windows at 4200-4230, 4435-4700 and 5100-5535 Å. Each of the ICA components is then divided by the power-law. An identical process is performed on each of the spectrum to be fitted, so that there is essentially zero shape in both the components and the spectrum to be fitted. The first six component weights are constrained to be non-negative, and the fit is done in logarithmic wavelength space, so that each pixel corresponds to a fixed velocity width.

1.3.5.2 *Quality of fits*

In general, the ICA components do a remarkably good job at reconstructing the spectra of the objects in our sample. For example, in J125141+080718 (discussed above), it does much better job at modelling the Fe II emission than the Boroson and Green, (1992) template. It is less sensitive to the spectral S/N, and the component weights do not need to be constrained. It is therefore much simpler to apply than fitting multiple Gaussians.

However, it does have its limitations. The components were calculated using a set of lower-redshift, lower-luminosity AGN, and quasar spectra are known to vary systematically as a function of luminosity. For example, the [O III] line is typically broader in more luminous quasars. Because there are so few objects with very broad [O III] in the low-redshift sample, the ICA reconstruction fails to reproduce the broadest [O III] profiles in our sample.

1.3.6 *Physical interpretation of ICA components*

Although the ICA analysis is not based on any physics, there appears to be a direct correspondence between the individual components and the different emission features which contribute to the spectra (Fig. 1.5). This correspondence is summarised in Table 1.2. The component w_1 seems to correspond to Fe II emission, the components w_2 and w_3 to broad H β emission, the components w_4 and w_5 to narrow [O III] emission at the systemic redshift, and the component w_6 to broad, blueshifted [O III] emission.

1.3.6.1 *Reconstructing the [O III] profile*

In order to measure non-parametric line parameters, e.g. v_{10} , we must first reconstruct the [O III] emission. It is fortunate that most of the [O III] emission is in just three of the ICA components; the remain-

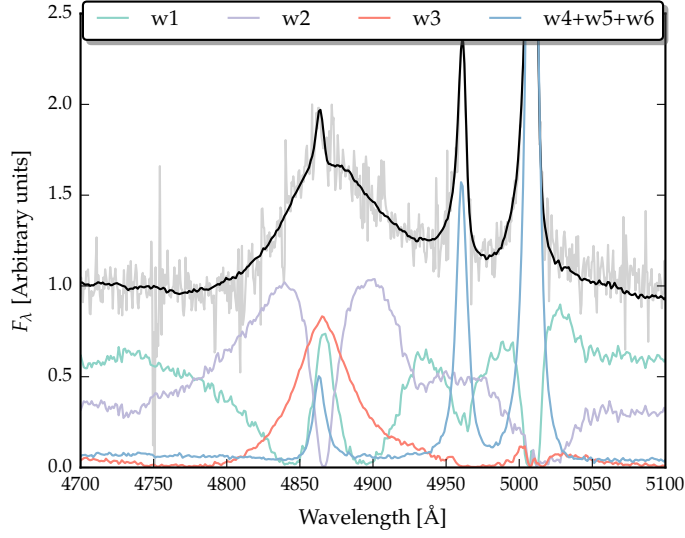


Figure 1.5: ICA reconstruction of J002952+020607. The ICA reconstruction is shown in black, and the spectrum in grey. The first three components, and the sum of components four, five and six are shown individually.

Table 1.2: Physical interpretation of the ICA components.

| Component | Origin |
|-----------|--------------|
| w_1 | Fe II |
| w_2 | H β |
| w_3 | H β |
| w_4 | [O III] core |
| w_5 | [O III] core |
| w_6 | [O III] wing |

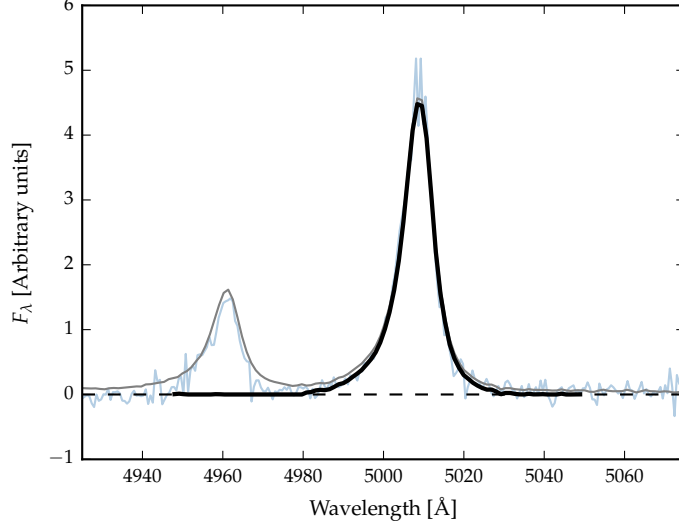


Figure 1.6: [O III] emission in J002952+020607. The data is shown in blue, and the ICA spectrum in grey. The first three ICA components have been subtracted from both the ICA composite and the data. The black curve shows the reconstructed [O III] profile (see text).

ing three contribute very little. Therefore, we can set the first three weights to zero to leave only the [O III] emission. The four correction components are also included.

We define the boundaries of [O III] λ 5008 as being between 4950 and 5500 Å. The blue limit is close to the peak of the [O III] λ 4960 line, and so to recover the intrinsic profile we instead use the blue wing of [O III] λ 4960. We use the emission from 4980-5050 Å, and from 4900-(4980-(5008.2-4960.3)). The blue window is then shifted by (5008.2-4960.3) to reconstruct the blue wing of the [O III] λ 5008 line. We then subtract a constant, because the flux does not always go to zero (suggests that there is probably flux which is not due to [O III] emission in components four to six).

The reconstructed spectra are shown in Figure ?? . At present I am summing the flux all the way from 4950 Å. However, this is quite a lot of flux to sum up, and we can't ascribe this flux to the wing of the [O III] emission with any certainty. This is borne out by the fact that there are quite large differences between, for example, v_{10} measured from the Gaussian fit and v_{10} measured from the ICA fit.

1.4 RESULTS

1.4.1 Gaussian fits

Our best-fitting profiles show a strongly blue-asymmetric profile (Fig. 1.7), with a significant fraction of the total emission in a blue

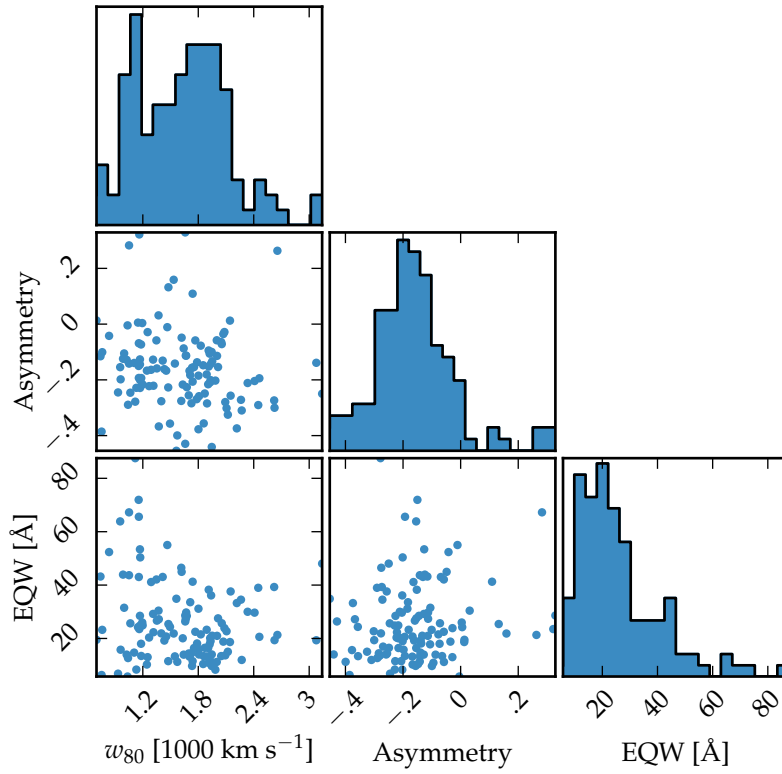


Figure 1.7: Correlations between w_{80} , R and EQW of [O III]. 119 objects are included: objects with low EQW, poor S/N, poor Fe II subtraction are not included. Objects for which [O III] is modelled using a single Gaussian are also excluded, because the asymmetry is always zero for these objects.

wing. The luminous blueshifted broad wing and the extremely broad profile reveals high-velocity outflowing ionized gas. Our results, and those of other authors, suggest that kpc-scale outflows in ionized gas are common among the most luminous high-redshift actively accreting SMBHs.

We see a correlation between the [O III] velocity width and blueshift. As the blueshift of the line increases it gets broader. This is consistent with Shen and Ho, (2014), where the strength of the narrow core is decreasing, leading to a broader and more blueshifted profile.

1.4.1.1 Eigenvector 1 correlations

At low redshifts, it is standard to use principle component analysis (PCA) to define quasar extrema. This has led to the so-called EV₁ correlates (Boroson and Green, 1992). Specifically, much of the variance in quasar spectra is reflected in an anti-correlation between the relative strength of Fe II and the H β FWHM. These emission line trends in the optical (for low- z quasars) can be extended to UV emission lines observed at higher redshifts. The C IV blueshift and EQW is a diagnostic that similarly spans the diversity of broad emission line properties in high redshift quasars (dominated by a virialized component at one extreme and a wind driven component at the other) (Richards et al., 2011; Sulentic et al., 2007). The similarity of the C IV EQW-blueshift parameter space at high redshift to EV₁ parameter space at low redshift suggests that these trends are connected.

Can we calculate a mapping between the two parameter spaces? As a first step we show how the EV₁ parameters change as a function of position in the C IV EQW-blueshift parameter space in Figure 1.8. Most of the diversity in C IV properties seems to be driven by the [O III] EQW. On the other hand, properties of the C IV line cannot be used to predict the H β FWHM. This is similar to what we found in Chapter ??: objects with large C IV blueshifts have narrow Balmer emission lines, but objects with modest C IV blueshifts have a wide range of Balmer line widths.

Can do something similar with ICA weights, but I'm not sure what the best question to ask is. Could make a linear model of the ICA component weights and fit to the C IV blueshift?

Because of this diversity, it is the dominant variable in the set of correlations making up EV₁, which is believed to be linked to certain fundamental parameters of the accretion process. In Figure 1.8 we show the [O III] EQW as a function of the H β FWHM and the optical Fe II strength. The optical Fe II strength is defined as the ratio of the Fe II and H β EQW, where the Fe II EQW is measured between 4434 and 4684Å. These parameters form part of EV₁, the first eigenvector in a principal component analysis which originated from the work of Boroson and Green, (1992). In our sample, these parameters follow

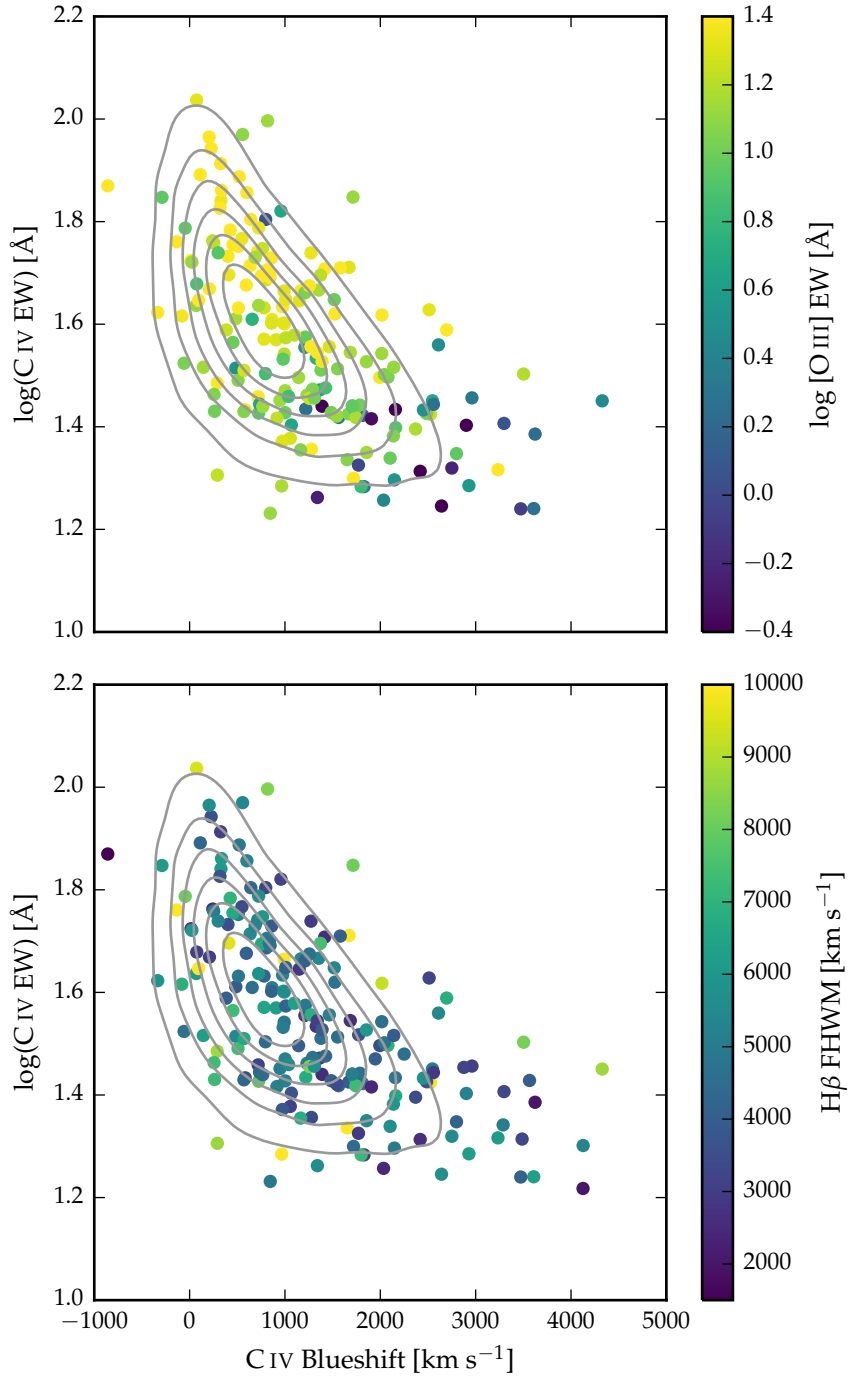


Figure 1.8: The high- z EV1 parameter space of C IV blueshift and EQW. Our sample is shown with points, and quasars from the full SDSS catalogue are shown with grey contours. The [O III] EQW varies systematically with position in the C IV blueshift-EQW parameter space (a) but H β FWHM shows significantly less systematic variation (b).

very similar correlations to what is observed at low- z (e.g. Shen and Ho, 2014). In particular, the anti-correlation between the [O III] and Fe II EQW.

Same as Shen, (2016), we confirm that the EV₁ correlations hold at high luminosities/redshifts. See also Sulentic et al. 2004, 2006; Runnoe et al. 2013. Make sure it's clear that Shen, (2016) quasars make up a significant chunk of our sample.

1.4.1.2 *Extreme [O III]*

Figure 1.9 shows the spectra of 18 objects which we visually identified as having exceptionally broad [O III] emission profiles. For all of these objects the [O III] emission is heavily blended. One consequence of this is that there is a significant degeneracy when the emission is decomposed in to individual contributions from Fe II, H β and [O III]. We note that there is a similarity between these objects and the four quasars presented in Zakamska et al., (2016).

1.4.2 *ICA fits*

We find there is a decreasing symmetric component at high luminosities. Relates directly to Shen and Ho, (2014). A stable narrow line region is removed by the outflowing material. Shen and Ho, (2014) showed that the strength of the core [O III] component decreases with quasar luminosity and optical Fe II strength faster than the wing component, leading to overall broader and more blueshifted profiles as luminosity and Fe II strength (or C IV blueshift) increases.

Zhang et al. 2011: Blueshift of [O III] correlates significantly with the EQW of the core. The more the peak of the line is blueshifted, the more the core component decreases dramatically, while the blue wing changes much less. We see this clearly in Figure 1.12. This is similar to behaviour of C IV? i.e. is there a mapping from this to the C IV space diagram? This would suggest that the mechanism producing the two correlations is the same. Consistent with the core coming from the canonical extended NLR where the gas is dominated by gravity of the bulge while the wing arises in an outflow. And C IV explained by wind. Suggests intimate connection between Broad line region (BLR) and NLR.

1.4.2.1 *Comparison of low- z and high- z samples*

In this section we compare the ICA component weights in our low- z and high- z samples.

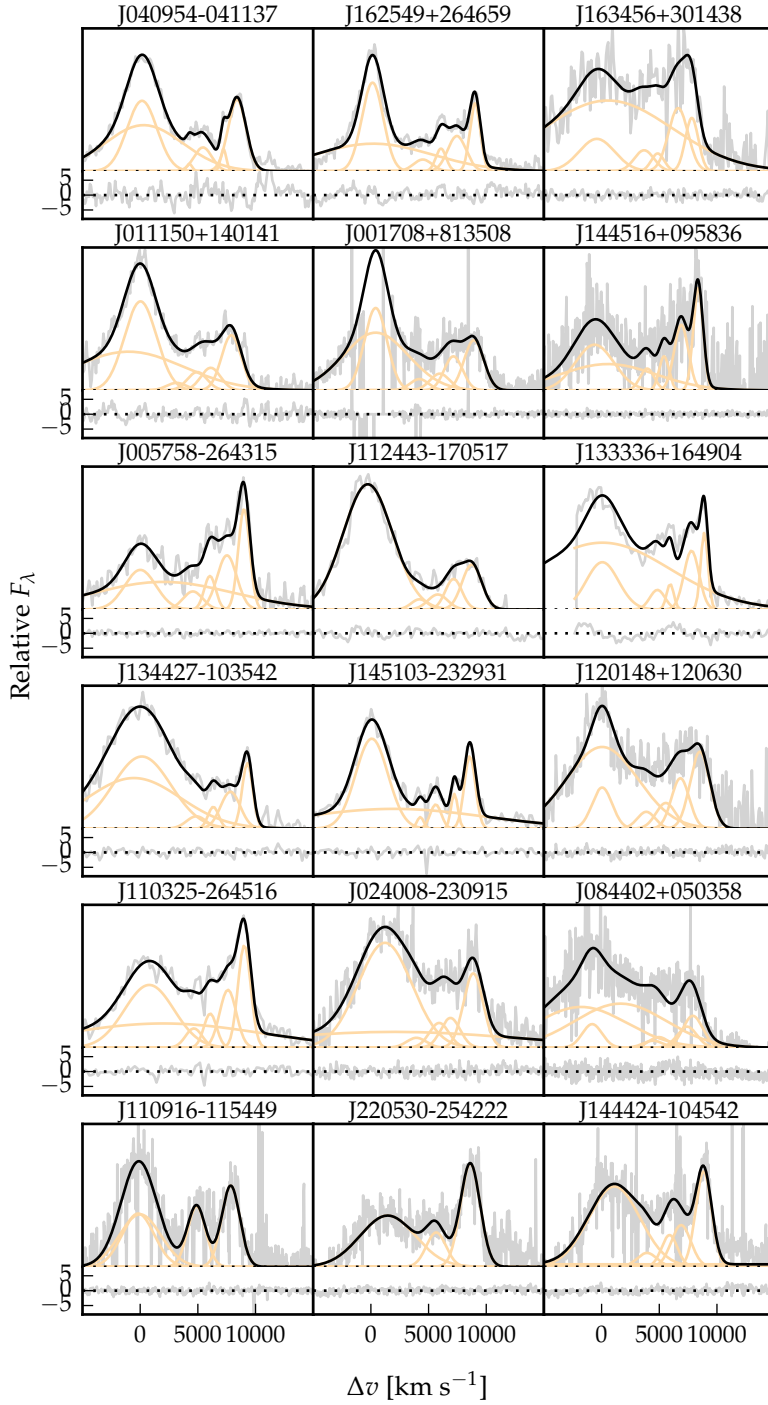


Figure 1.9: Multi-component Gaussian fits to the continuum-subtracted $H\beta/[O\text{ III}]$ emission in 18 quasars with extreme $[O\text{ III}]$ emission profiles.

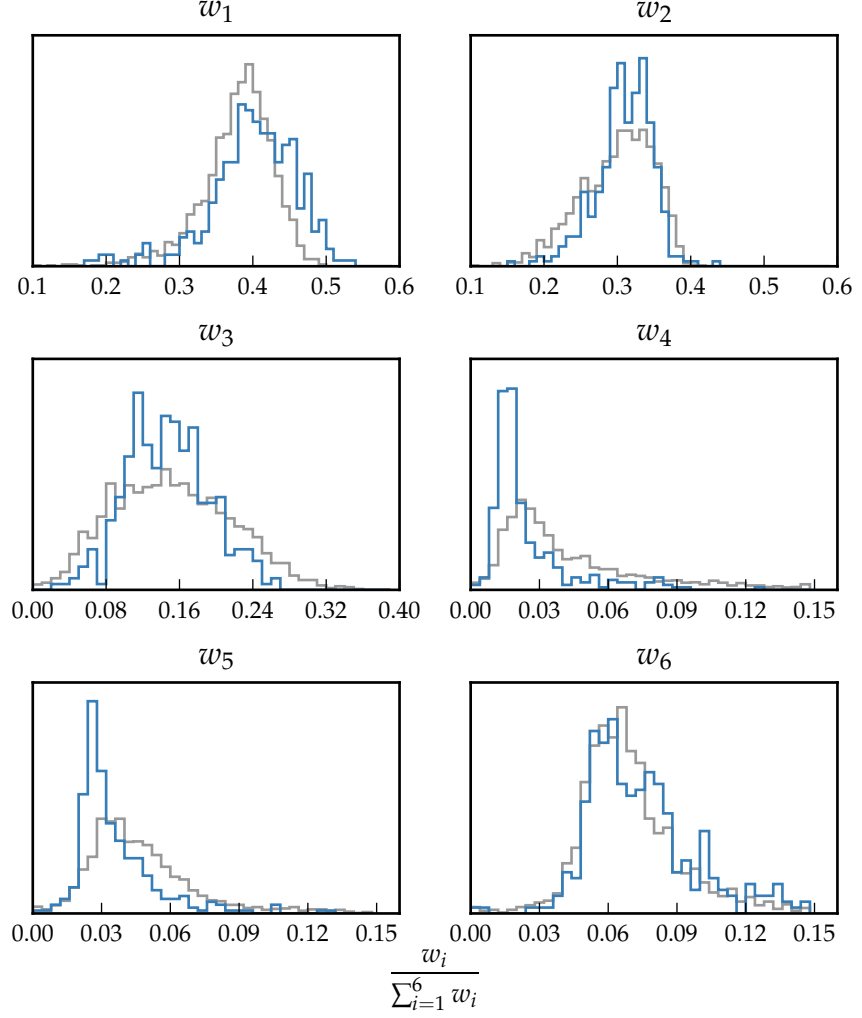


Figure 1.10: The relative weight in each of the six positive ICA components for the high-luminosity (blue) and low luminosity samples (grey). In the high-luminosity sample Fe II emission is stronger (component w_1). The core [O III] emission (components w_4 , w_5) is weaker but the strength of the blueshifted wing (w_6) is the same.

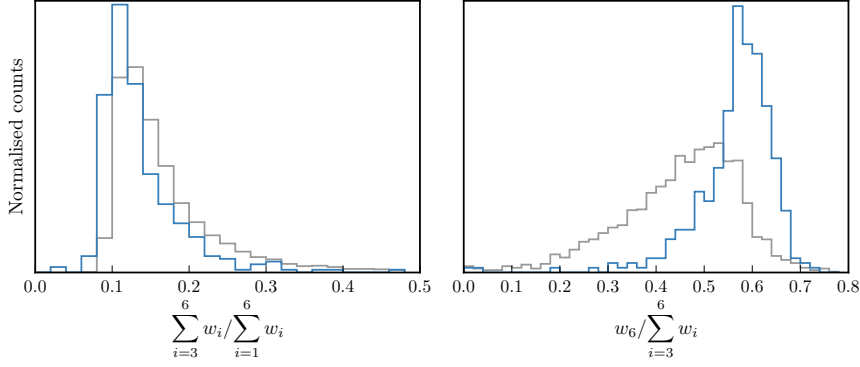


Figure 1.11: The relative weight in the three ICA components corresponding to [O III] emission (*left*) and the relative weight of the component most closely related to blueshifted [O III] emission relative to all three [O III] components (*right*). [O III] emission is weaker in the high-luminosity sample, but the relative contribution from the blueshifted component to the total [O III] emission is higher.

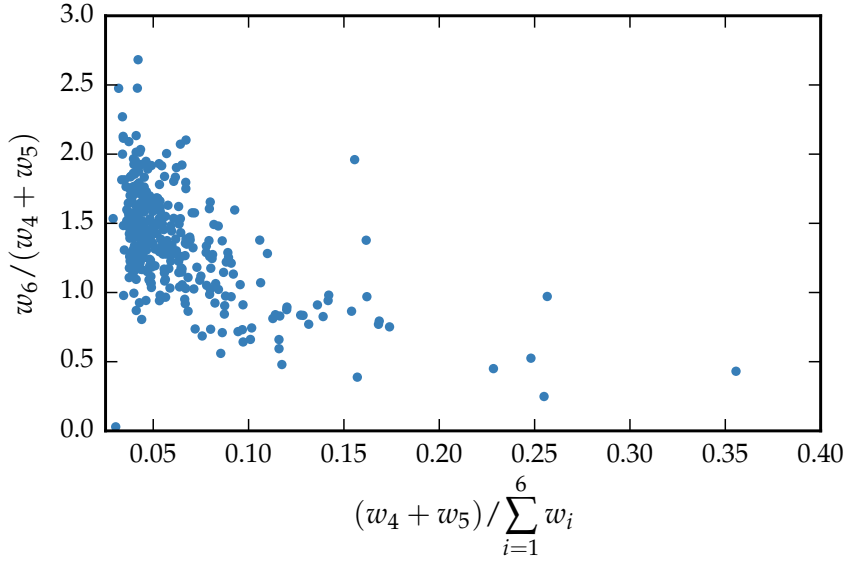


Figure 1.12: Anti-correlation between the relative contribution from the wing to the total [O III] profile and the strength of the core.

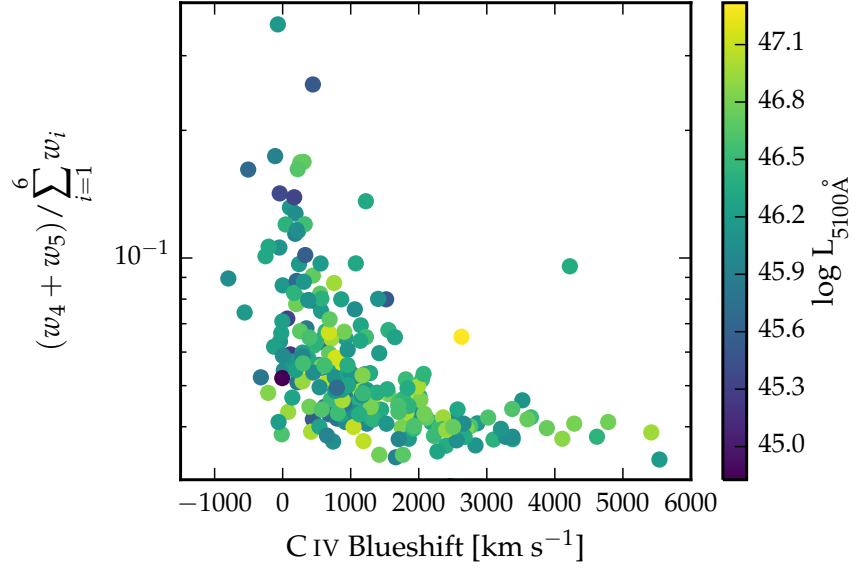


Figure 1.13: The strength of core [O III] as a function of the C IV blueshift. The C IV blueshift is measured relative to the NIR ICA redshift.

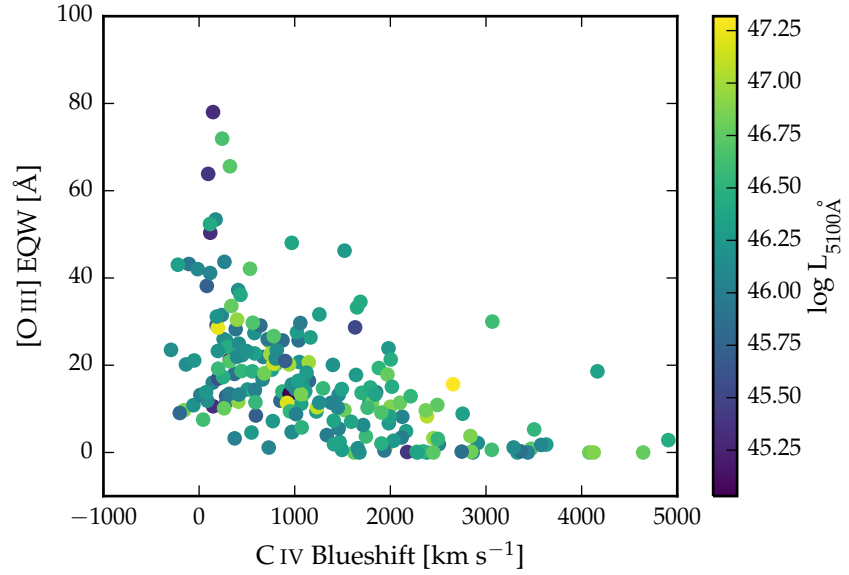


Figure 1.14: The strength [O III] EQW as a function of the C IV blueshift. The C IV blueshift is measured relative to the NIR ICA redshift.

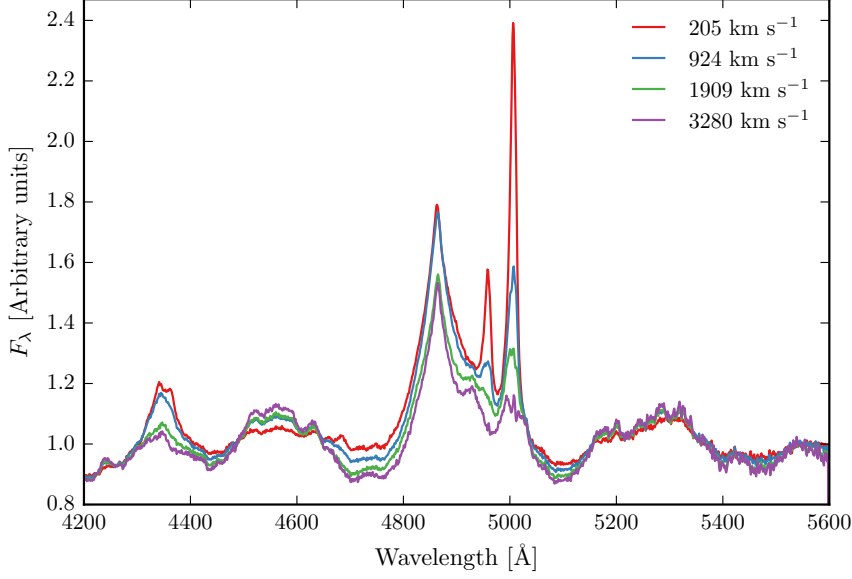


Figure 1.15: Median ICA-reconstructed spectra as a function of the C IV blueshift.

1.4.2.2 *EV₁ correlations*

In Figure 1.13 we show how the [O III] strength varies as a function of the C IV blueshift. There is a very well defined relation: when C IV is strongly blueshifted [O III] is very weak. Is the AGN NLR absent in objects where outflows have reached kiloparsec scales, sweeping up the low-density material responsible for the [O III]-emission? If the BLR outflows can escape, they are very fast and wouldn't need long to clear out the NLR gas.

This is shown in a different way in Figure 1.15. Here we divide our sample in to four bins according to the C IV blueshift. From the quasars in each C IV blueshift bin we then find then generate an ICA spectrum using the median weights from each quasar. The differences in the spectra as a function of the C IV blueshift are dramatic. [O III] becomes progressively weaker and more blueshifted. The anti-correlation with Fe III and the blueward Fe II also clear, but there is no change in the redward Fe II.

This seems to really connect high-*z* EV₁ with low-*z* EV₁, which I don't think has really been done before. At low redshifts we have the strengths of [O III], Fe II, and the H β FWHM. At high redshifts we have the C IV blueshift and EQW. The distribution of quasars in these two planes look qualitatively similar. It's tempting to think that quasars with large C IV blueshifts should also have strong Fe II and weak [O III]. This is indeed what our results seem to suggest.

The ICA can be thought of as update on EV₁. The spectral diversity is encapsulated in the EV₁ components. Most of the variance in EV₁

is the anti-correlation between the strengths of [O III] and Fe II. So at one end we have objects with strong Fe II and weak [O III], and at the other end objects with weak Fe II and strong [O III]. Other properties, including the C IV blueshift and the H β FWHM, also change systematically. Our work shows that the ICA component weights change systematically along the EV₁ sequence. .

*What is the best way
to actually do this
mapping?*

1.5 MEASURING THE QUASAR SYSTEMIC REDSHIFT

In this section we do a comparison of systemic redshift estimates from [O III], broad H β and H α , and from fitting the ICA component weights. This is an important issue. Accurate systemic redshift estimates are essential in a number of applications, and researchers have devoted a large amount of telescope time to obtaining near-infrared spectra to access [O III] for this purpose. HI, CO and absorption line measures of the host galaxy rest frame suggest that [O III] usually gives consistent results within 200 km/s (de Robertis 1985; Whittle 1985; Wilson & Heckman 1985; Condon et al. 1985; Stripe 1990; Alloin et al. 1992; Evans et al. 2001). However, our work shows that at high luminosities this can result in large errors (profile can be dominated by blueshifted component, Fe emission can be improperly subtracted, or [O III] might not be detected at all).

1.5.1 H α

There are 224 quasars in our sample with spectra covering the H α emission line. We discard seven of these from our sample because of very low S/N (<2.5 measured in the H α line), leaving 217. To measure the position of the line we fit a parametric model, which is very similar to the model described in Chapter ???. The continuum emission is first modeled and subtracted using the procedure described in Chapter ???. We then test five different models with increasing degrees of freedom to model the H α emission. The models are summarised in Table 1.3. They are (1) a single broad Gaussian; (2) two broad Gaussians with identical velocity centroids; (3) two broad Gaussians with different velocity centroids; (4) two broad Gaussians with identical velocity centroids, and additional narrower Gaussians to model the narrow H α emission, and the narrow components of [N II] $\lambda\lambda 6548, 6584$ and [S II] $\lambda\lambda 6717, 6731$; (5) two broad Gaussians with different velocity centroids, and additional narrower Gaussians. If used, the width and velocity of all narrow components are set to be equal in the fit, and the relative flux ratio of the two [N II] components is fixed at the expected value of 2.96. The model we select is the simplest model for which the fractional change in the reduced chi-squared from the model with the lowest reduced chi-squared is less than ten per cent. The redshift is

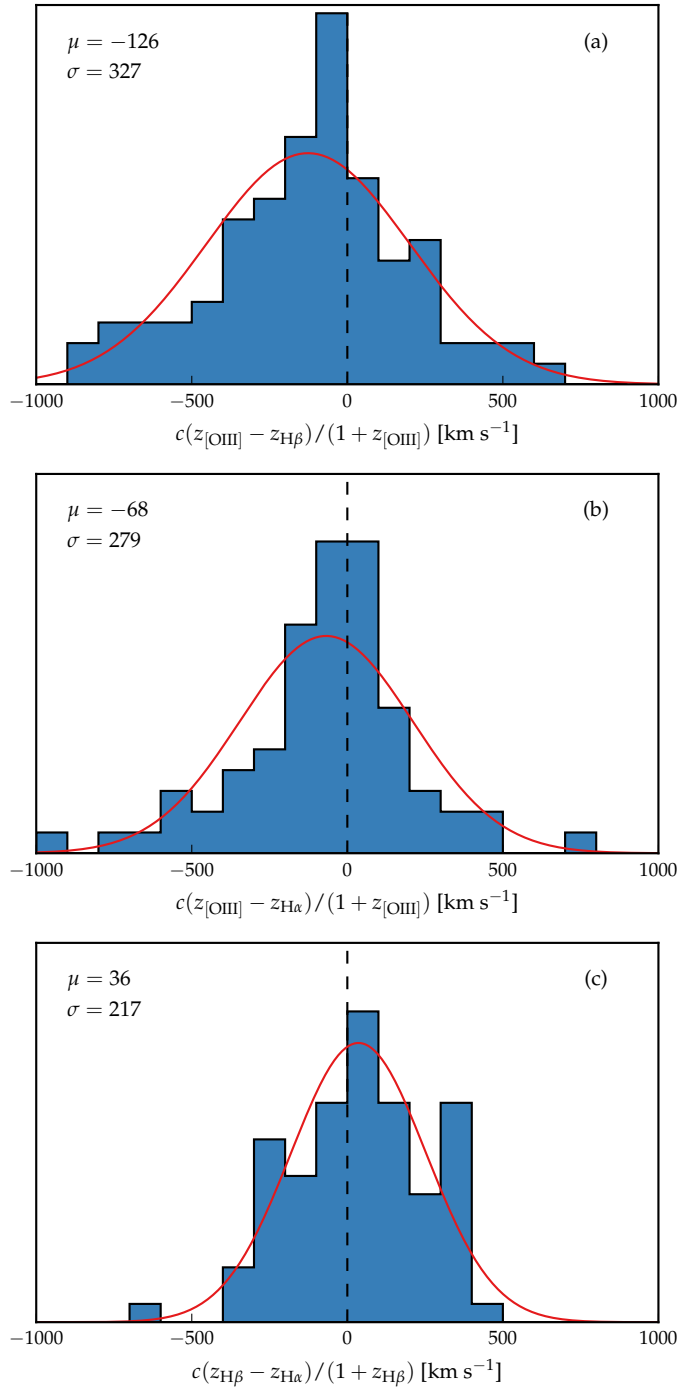


Figure 1.16: Comparison of systemic redshift estimates using [O III], broad $\text{H}\beta$ and broad $\text{H}\alpha$. In all cases the line location is defined as the peak wavelength of the best-fitting model. There are 93, 73 and 83 objects in (a), (b) and (c) respectively. The mean and standard deviation have been calculated by fitting a Gaussian function to the distribution. **Need to look at flags>1 for $\text{H}\alpha$ and $\text{H}\beta$. Is peak around zero in (a) real?**

Table 1.3: Models used for H α emission

| Model | Components | Fix centroids? | Number |
|-------|--------------------------------------|----------------|--------|
| 1 | 1 broad Gaussian | N/A | 10 |
| 2 | 2 broad Gaussians | Yes | 71 |
| 3 | 2 broad Gaussians | No | 32 |
| 4 | 2 broad Gaussians + narrow Gaussians | Yes | 51 |
| 5 | 2 broad Gaussians + narrow Gaussians | No | 53 |

then measured at the peak flux of the H α model, including both the broad and narrow components of H α if appropriate.

1.5.2 ICA

Benefit of ICA is that it works regardless of the [O III] strength.

Can also describe what I found trying to get redshifts from broad H α , H β ? (Narrow components generally very weak at these luminosities so can't be used.) Generally find no systematic errors but large ($\sim 1000 \text{ km s}^{-1}$ scatter). Comparing NIR ICA to [O III] for the [O III] with high S/N I find small (few hundred km s^{-1}) scatter.

1.6 LUMINOSITY/REDSHIFT-EVOLUTION OF [O III] PROPERTIES

In this section we look for any luminosity/redshift dependent changes in the [O III] line properties. To do this we extend the dynamic range of our samples in terms of both luminosity and redshift by supplementing our sample with quasars presented by Zakamska and Greene, (2014) and Harrison et al., (2016).

The Zakamska and Greene, (2014) objects are a sample of 568 obscured luminous quasars selected from SDSS (Reyes et al., 2008; Yuan, Strauss, and Zakamska, 2016). They are selected to have [O III] luminosities above $10^{8.5} L_{\odot}$ and have a median redshift $z = 0.397$.

We also include 40 quasars at redshifts $1.1 \leq z \leq 1.7$ from the KMOS AGN Survey at High redshift (KASHz) with [O III] line measurements.

We also have the same information for $\sim 20\,000$ SDSS spectra from Mullaney et al., (2013).

In Figure 1.17 we show the [O III] velocity width as a function of the [O III] luminosity and the quasar redshift. The lack of any redshift-evolution between $z = 0$ and $z = 1.5$ was reported by Harrison et al., (2016). Our additional data suggests that this continues to $z \sim 2.5$. On the other hand, at fixed redshift, we see a significant correlation between the [O III] velocity width and the luminosity.

The fact that we don't see many broad lines in the Zakamska and Greene, (2014) objects even at luminosities $> 43 \text{ erg/s}$ could be due

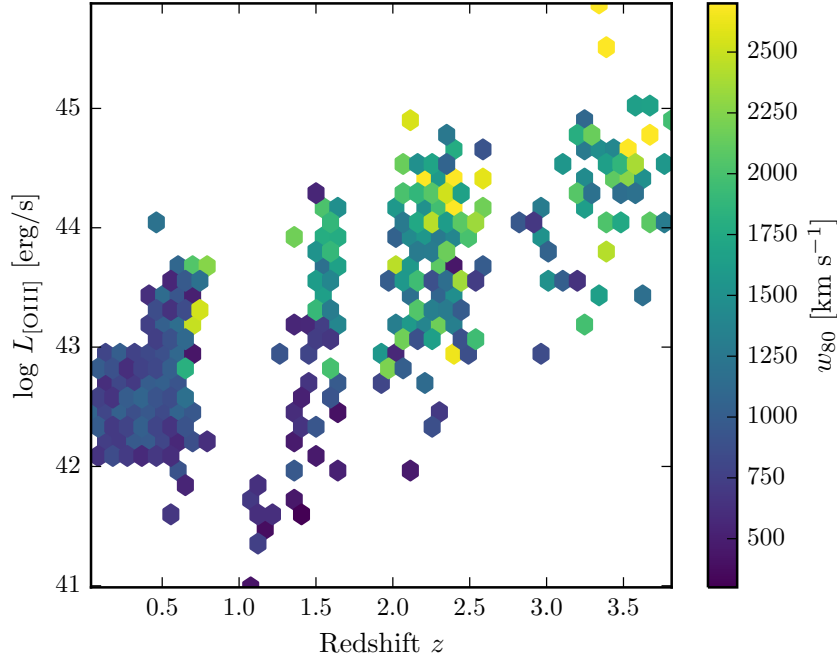


Figure 1.17: The [O III] velocity-width, characterised by w_{80} , as a function the [O III] luminosity and the quasar redshift. The color of each hexagon denotes the mean w_{80} for the objects in that luminosity-redshift bin. We have supplemented our sample with low- z objects from Zakamska and Greene, (2014) and medium ($z \sim 1.5$) redshift objects from Harrison et al., (2016). If I keep this plot make sure its clear which points belong to which sample.

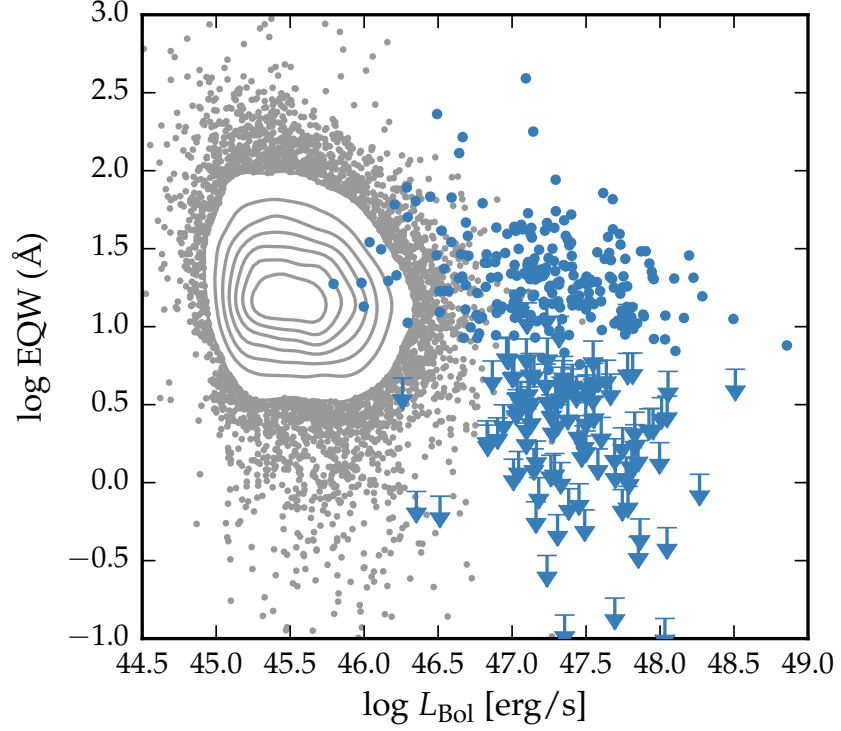


Figure 1.18: The [O III] EW as a function of the quasar bolometric luminosity for the sample presented in this chapter (blue circles) and the low- z SDSS sample (grey points and contours). Upper limits are denoted by the downward arrows.

to the fact that these are all type II quasars, whereas the sample presented in this chapter are all type I. Mullaney et al., (2013) showed that the [O III] lines of type I quasars are typically broader than in type II quasars.

1.7 EQUIVALENT WIDTH

Firstly, the best-fitting model comprising the continuum, Fe II, and H β emission is subtracted from the spectra, leaving behind only emission due to [O III]. From this spectra we generate 100 mock spectra, where the flux at each wavelength is randomly drawn from a Normal distribution with a mean equal to the flux convolved with a Gaussian of width 200 km s^{-1} and a width equal to the known error. We then perform an error-weighted linear least-squares regression with an [O III] template derived from a fit to a very high S/N low redshift SDSS composite spectra. The equivalent width of the best-fitting model is recorded for each of the 100 realisations of the spectra. The error in the equivalent width is defined as the root-mean-square of these values.

In Fig. 1.18 we show the $[\text{O III}]\lambda 5008$ EW as a function of the quasar bolometric luminosity. Bolometric luminosity is estimated from the monochromatic continuum luminosity at 5100\AA using the correction factor given by Richards et al., (2006). For comparison, we also show the low- z sample from Shen et al., (2011).

The equivalent width of $[\text{O III}]$ has been found to strongly decrease as a function of redshift and/or luminosity (e.g. Brotherton, 1996; Netzer et al., 2004; Sulentic et al., 2004; Baskin and Laor, 2005).

The size of the narrow line region is roughly expected to scale as $L^{0.5}$ (e.g. Netzer et al., 2004). However, for high luminosity quasars with strong $[\text{O III}]$ this gives NLR sizes which are unreasonably large (~ 100 kpc; Netzer et al., 2004).

Netzer et al., (2004) found 1/3 of their high luminosity sample had very weak $[\text{O III}]$, whereas quasars with weak $[\text{O III}]$ are very rare for nearby AGN. We find that $[\text{O III}]$ is undetected/very weak in XX per cent of our sample, which is very similar to the fraction reported by Netzer et al., (2004). Netzer et al., (2004) claim that for the population of strong $[\text{O III}]$ emitters there is no reduction of EW with increasing source luminosity. On the other hand, there are many weak or no $[\text{O III}]$ emitters at high luminosity that could give the impression that the line EQW decreases with increasing source luminosity.

1.7.1 $[\text{O III}]$ and C IV outflows are linked

Optical spectra are available for XXX quasars in our catalogue, and cover the broad C IV doublet. As we described in Chapter ??, C IV is often blueshifted, which almost certainly signal the presence of strong outflows, most likely originating in a disc wind. In Chapter ?? we demonstrated that the quasars in our sample cover the full range of C IV blueshifts seen in the SDSS quasar population, which makes our sample unique in that it allows us to study properties of the quasar across the full parameter range.

The C IV velocity centroid measurements are taken directly from Chapter ?. We define the ‘location’ of the $[\text{O III}]$ emission using v_{10} , although the results are the same if v_{20} , v_{50} etc. are used instead. The $[\text{O III}]$ is therefore very tightly correlated with the $[\text{O III}]$ width, except for the asymmetry.

In Figure 1.19 we show the C IV blueshifts against the $[\text{O III}]$ blueshifts. This comparison is done for a sub-sample of 146 objects where we have good measurements of the C IV, $[\text{O III}]$ profiles.

There is a clear and strong correlation. Note that our EQW cut removes most of the quasars with large C IV blueshifts, since $[\text{O III}]$ is on average very weak in these quasars. Similar correlations have been tentatively found in lower redshift quasars and AGN (Zamanov et al., 2002).

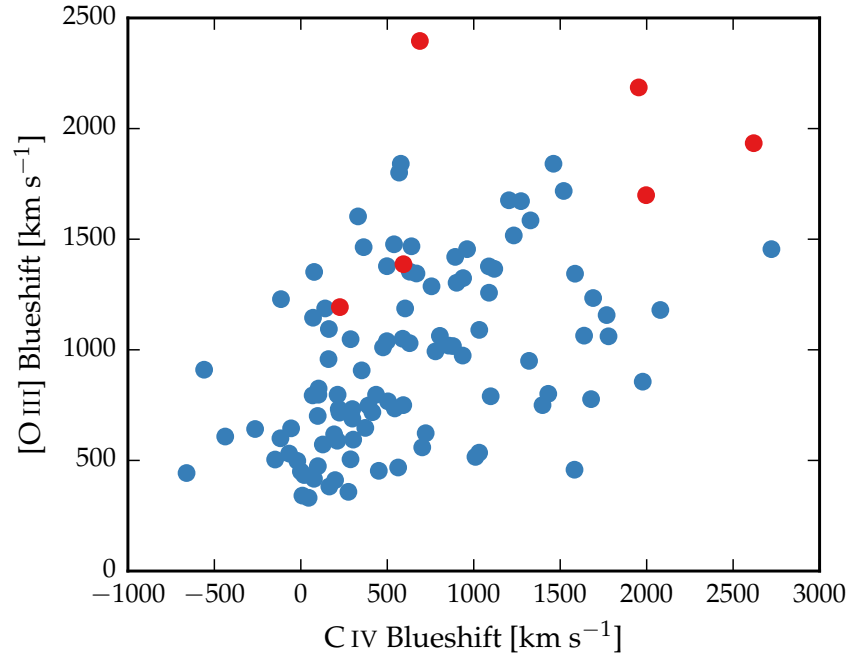


Figure 1.19: The relation between the blueshifts of C IV and [O III]. Note that we are using v_{10} for the [O III] position and v_{50} for the C IV position. We can't use v_{50} for [O III] because sometimes we are using a single Gaussian, especially if the [O III] is weaker and we miss the broad component.

The blueshifting of C IV is known to correlate with luminosity (Richards et al., 2011). In [O III], the blueshifted wing becomes relatively more prominent as the luminosity of the quasar increases (Shen and Ho, 2014). Therefore, it is plausible that the correlation between the C IV and [O III] blueshifts is a secondary effect that is driven by the correlation of each with the luminosity. However, no strong luminosity-dependent trends are apparent in Figure 1.19. We find that both the [O III] and C IV blueshifts are correlated with the luminosity, but that these correlations are much weaker than the correlation between the [O III] and C IV blueshifts.

1.8 EIGENVECTOR ONE CORRELATIONS

1.9 BROAD ABSORPTION LINE QUASARS

19 quasars in our catalogue are classified as broad absorption line (BAL) quasars, using either the SDSS classification flags or the Allen et al., (2011) catalogue. We find that the BAL quasars have typically broader [O III] than the rest of the sample. Note that in the Zakamska et al., (2016) sample of very red quasars, the incidence of BALs is very high, and these objects have extremely broad [O III] profiles. A two-sided Kolmogorov-Smirnov statistic on the w_{80} distributions returned a p-value of 0.10. What does this mean? Try with different parameters? Histograms look rubbish so maybe just give the numbers.

Check all of this

1.10 DISCUSSION

Looking at the [O III] velocity width as a function of luminosity tells us about the physical drivers of the outflows observed in [O III]. The correlation with luminosity suggests that the highest velocity outflows are associated with the most luminous AGN. This has been reported for low-redshift AGN, for both ionized and molecular outflows (e.g. Westmoquette et al. 2012; Veilleux et al. 2013; Arribas et al. 2014; Ciccone et al. 2014; Hill & Zakamska 2014).

This suggests that the outflows are driven by radiative forces. On the other hand, Mullaney et al., (2013) find that once the correlation between the [O III] luminosity and the radio luminosity has been taken in to account, the [O III] velocity width is more strongly related to the radio luminosity of the AGN.

1.10.1 Type II quasars

Implications of our findings on searches for high-redshift type 2 quasars. It could be that type II quasars exist. If you look at CIV/MgII the narrow line components are very weak. So the contribution from

the narrow line region is very weak in luminous quasars, and you just won't see it even if the broad line region is obscured. Findings in this paper seem to suggest that the startic narrow line region is very weak in luminous quasars.